nature sustainability

Article

https://doi.org/10.1038/s41893-025-01755-x

Energy-efficient indirect (bi)carbonate electroreduction in a porous solid electrolyte reactor

Received: 20 March 2025

Accepted: 9 December 2025

Published online: 07 January 2026

Check for updates

Valery Okatenko[1], Ahmad Elgazzar[1], Anna Loiudice[2], Raffaella Buonsanti[2] & Haotian Wang[1,3,4,5,6]

Carbon capture, recovery and conversion are typically done by three separate steps, which notably increases the total energy consumption and capital costs. Here we propose to indirectly convert (bi)carbonates, which are carbon-rich sorbents in alkaline carbon capture, into valuable chemicals in a porous solid electrolyte (PSE) electrochemical CO_2 reduction (CO_2RR) reactor while eliminating the energy-intensive CO_2 recovery step. Specifically, direct feeding of (bi)carbonates into the PSE layer while performing CO_2RR allows simultaneous CO_2 regeneration within the PSE chamber. Impressive electrochemical performance was demonstrated, with up to 96% formate Faradaic efficiency, 95% CO_2 recovery efficiency and 86% bicarbonate-to-formate conversion. Reactor versatility allowed us to obtain up to 5.0 M formate, ~50% higher than bicarbonate solubility and C_{2+} products with 73% selectivity, setting the state of the art for bicarbonate-fed CO_2RR. Operating for at least 100 hours at 100 mA cm^{-2} averaging 82% CO_2 recovery and 89% Faradaic efficiencies, our reactor adds economic value to alkaline carbon capture and CO_2 conversion, bringing both closer to practical implementation.

Carbon capture, utilization and storage (CCUS) approaches are critical for the efforts to meet the climate targets[1]. To make CCUS commensurate with the climate change mitigation scale, most of the captured carbon must be permanently sequestered[2]. At the same time, captured carbon utilization is crucial to enable the circular economy and to facilitate the CCUS adoption[2].

In a typical industrial framework, carbon capture, recovery and downstream conversion are independent[3], leading to high energy and capital costs[4]. For example, CO_2 capture with alkaline aqueous solutions, an established approach featuring high stability and scalability[5], relies on energy-intensive calcination to recover CO_2 from the capture solution (Fig. 1a)[6]. More recently, approaches that mostly rely on the use of sharp pH gradients in the electrodialysis cell have been introduced to recover CO_2 from its aqueous solutions[7–12]. This enables lower energy consumption, bringing it to about 3 GJ ton^{-1}_{CO2} for electrodialysis compared to 6–10 GJ ton^{-1}_{CO2} for calcination[4,6,9]. However, using electrodialysis or electrochemical cell for CO_2 recovery still implies building and operating separate recovery and conversion electrolysers. Non-aqueous CO_2 capture and recovery approaches also require 3–7 GJ ton^{-1}_{CO2} for the recovery step[4].

These facts inspired research combining the carbon recovery and utilization steps in a single device, offering to save 11–44% of the total energy and capital costs compared to sequential recovery and conversion[4]. Electrochemical approaches have recently emerged as powerful tools extending beyond independent CO_2 capture, recovery and conversion (CO_2 reduction reaction, CO_2RR) towards direct conversion of

[1]Department of Chemical and Biomolecular Engineering, Rice University, Houston, TX, USA. [2]Laboratory of Nanochemistry for Energy, Institute of Chemical Sciences and Engineering, École Polytechnique Fédérale de Lausanne, Sion, Switzerland. [3]Department of Materials Science and NanoEngineering, Rice University, Houston, TX, USA. [4]Department of Chemistry, Rice University, Houston, TX, USA. [5]Rice Advanced Materials Institute, Rice University, Houston, TX, USA. [6]The Rice Water Institute, Rice University, Houston, TX, USA. e-mail: htwang@rice.edu

https://doi.org/10.1038/s41893-025-01755-x

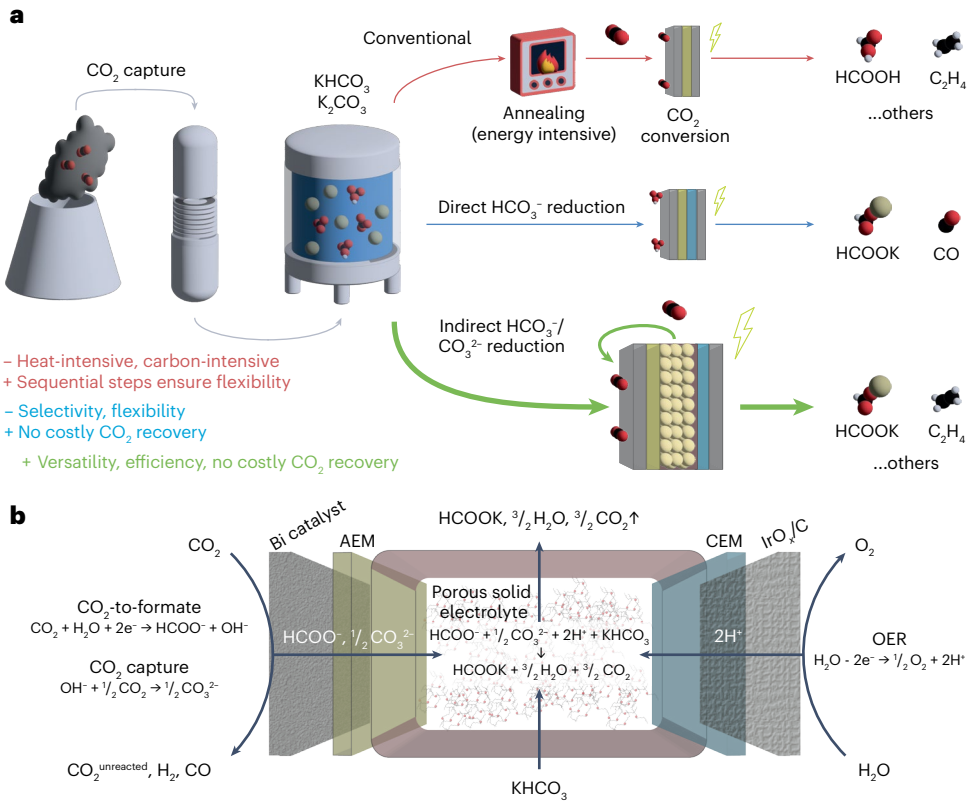

Fig. 1 | Comparison of strategies to recover and convert CO_2 from $KHCO_3$/K_2CO_3 capture solutions and the proposed indirect HCO_3^- reduction reactor design. a, Overview of different carbon capture and conversion frameworks, their benefits and drawbacks (high heat and energy demand of annealing and fine balance in the direct HCO_3^- reduction process chemistry, where in situ CO_2 recovery and its conversion must occur in the same location). The use of single-unit CO_2 recovery and conversion unit combines the benefits of both without their main drawbacks. **b**, Illustration of the CO_2-to-formate three-chamber PSE reactor for recovery of CO_2 from $KHCO_3$ solution. This scheme highlights that CO_2 recovery takes place in the middle chamber, while its conversion takes place at the cathode which allows for independent optimization of both processes and maximizes overall efficiency.

carbon capture outlets into products (reactive carbon capture, RCC) (Fig. 1a)[11,13–24]. Yet despite its potential, RCC needs improvements to be practically viable[4]. RCC with organic sorbents often suffer from low selectivity, mass transport limiting process rates and vulnerability to contaminants[13–18,25]. Direct HCO_3^- reduction imposes strict limitations on $KHCO_3$ concentrations, struggles to exceed about 70% selectivity and cannot efficiently utilize K_2CO_3[23,26–28], which is the component of KOH-assisted carbon capture units output[29,30].

Here we propose a strategy to convert bicarbonate into product in the porous solid electrolyte (PSE) reactor without a separate CO_2 recovery step. Simultaneously with CO_2RR at the cathode (for example, to $HCOO^-$), gas-phase CO_2 is recovered from bicarbonate (HCO_3^-) in the PSE layer, allowing indirect electrochemical conversion of (bi)carbonate to formate. Meanwhile, CO_2 absorbed by the alkaline interface in conventional CO_2 electrolyser can be recovered in the PSE layer of our reactor, yielding 78% carbon-to-formate single-pass conversion efficiency. We achieve this by using the continuous proton flux in the PSE layer from the anode reaction[31,32], which we react with supplied carbon-containing solution and efficiently recover CO_2 (Fig. 1b). This design offers the unique advantage of fully leveraging the molecular transformation and ionic transport in the PSE reactor for integrated CO_2 conversion and regeneration steps, while not sacrificing the performance of each step (Fig. 1a). Our design can utilize carbonates as CO_2 source, which allows flexibility in the upstream carbon capture step regarding the sorbent composition end states[23,30]. The electrolyser can operate both in the flow and in batch configuration, and it is able to continuously recover CO_2 for 100 h at 100 mA cm^{-2}. Its modular architecture allowed us to develop four-chamber PSE reactor design and deliver formate with concentrations exceeding bicarbonate solubility limit, along with C_{2+} products with high selectivity using bicarbonate as the sole carbon supply. These results pave the way for further development and practical implementation of PSE reactors for integrated CO_2 recovery and conversion.

Results

CO_2 recovery approach validation and its stoichiometry

The operating principle of the CO_2-to-formate PSE reactor for CO_2 recovery from the carbon capture $KHCO_3$ and K_2CO_3 solutions is presented in Fig. 1b and Supplementary Fig. 1. It consists of a cathode performing CO_2RR to formate, a middle chamber packed with the PSE for ionic conductivity and an anode performing oxygen evolution reaction (OER). We used commercial Bi_2O_3 nanoparticles sprayed onto gas diffusion electrode (GDE) as cathode and commercial IrO_2 GDE as anode[33]. Anion-exchange (AEM) and cation-exchange (CEM) membranes separated the middle chamber from the electrodes, and carbon capture solution, $KHCO_3$ or K_2CO_3, was continuously supplied to the middle layer for CO_2 recovery. This design minimizes the carbon losses in conventional CO_2RR electrolyser system and allows >90% carbon utilization[34], which is crucial for the practical CO_2RR implementation.

We compared the reactor operation with H_2O and 0.1 M $KHCO_3$ as middle-layer solutions (Fig. 2a, Supplementary Figs. 2 and 3 and Supplementary Notes 1 and 2). We obtained formate Faradaic efficiency (FE_{HCOO^-}) of about 95% for both (Fig. 2b), comparable with the state of the art[31,32,34,35] and indicating that 0.1 M $KHCO_3$ does not negatively affect the catalyst. As we designed a set-up to detect the recovered CO_2 in the middle layer (Supplementary Figs. 4 and 5), we obtained 0.47 ml min^{-1} cm^{-2} CO_2 with H_2O supply at 150 mA cm^{-2} (Fig. 2c), closely matching the earlier report[32]. This CO_2 originates from CO_2 capture at the cathode/

https://doi.org/10.1038/s41893-025-01755-x

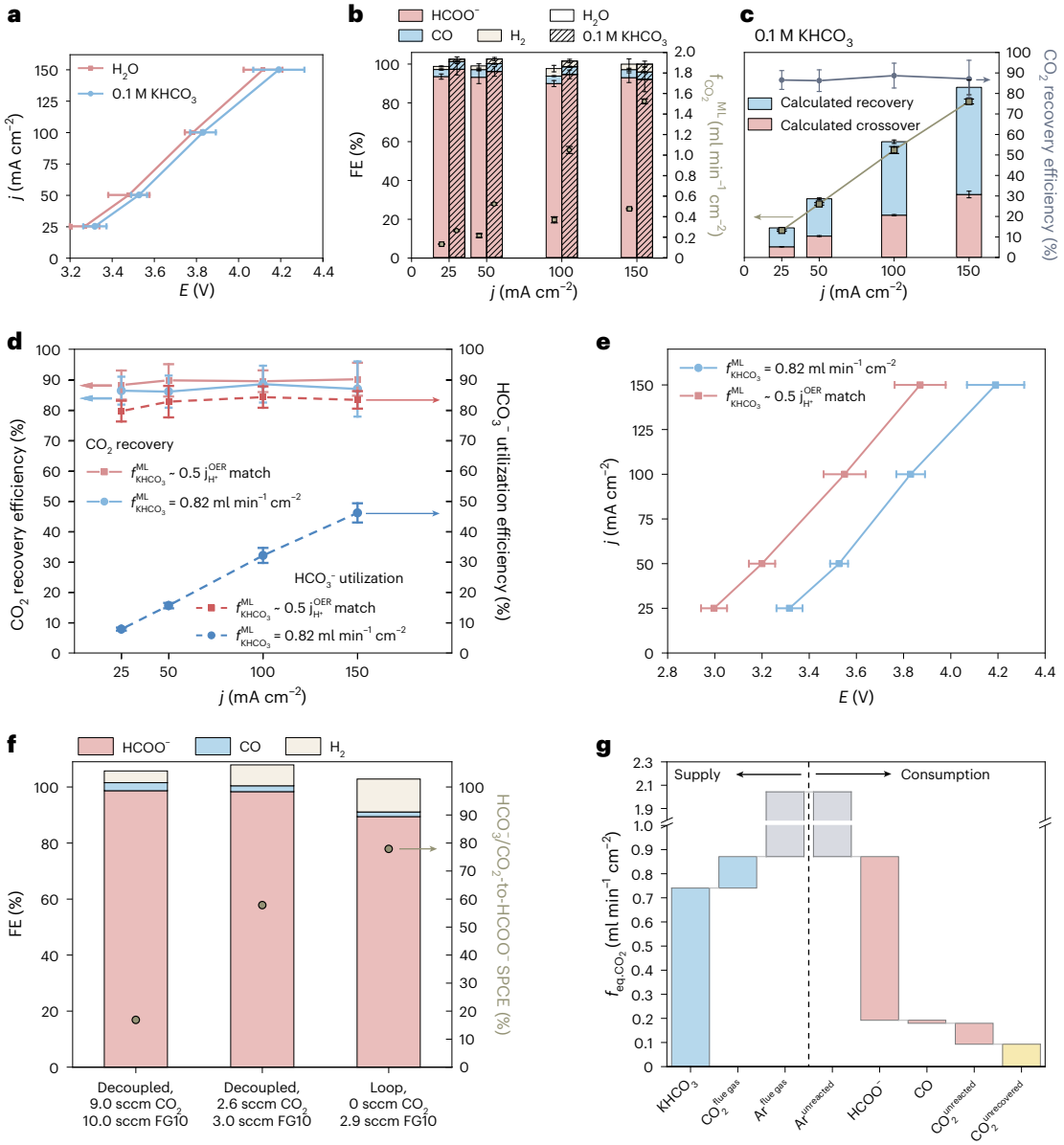

Fig. 2 | Experimental validation of the concept, impact of 0.1 M $KHCO_3$ flow rate and physical CO_2 looping demonstration. a, The *I*–*V* (current density–voltage) curve of the CO_2-to-formate PSE reactor with H_2O and 0.1 M $KHCO_3$ middle-layer solutions. **b**, Faradaic efficiencies and CO_2 detected in the middle-layer outlet with H_2O and 0.1 M $KHCO_3$ as feeding solutions. The results indicate comparable FE_{HCOO^-} in two cases and about three times higher CO_2 in the middle-layer outlet supplied with 0.1 M $KHCO_3$ compared to H_2O, validating the recovery approach. **c**, CO_2 detected in the middle-layer outlet, calculated values of crossover and recovered CO_2 and CO_2 recovery efficiency with 0.1 M $KHCO_3$ middle-layer solution. The amount of detected CO_2 is close to the calculated values. **d**,**e**, CO_2 recovery and HCO_3^- utilization efficiency (**d**) and *I*–*V* curves for 0.1 M $KHCO_3$ supplied at fixed rate and with matching between the middle-layer solution flow rate and the anticipated rate of free H^+ generation (molar equivalent of 0.5 $j_{H^+}^{OER}$) (**e**). The matching demonstrates improvement of both metrics at all applied currents. **f**, Faradaic and single-pass conversion efficiencies of carbon entering the reactor to formate at 100 mA cm^{-2} with 0.1 M $KHCO_3$ at flow rate of 0.68 ml min^{-1} and different supply configurations (FG10 stands for 10% CO_2–90% Ar simulated flue gas). The results suggest there is only minor FE_{HCOO^-} decrease upon transition from decoupled to loop operation. **g**, Full carbon balance of the reactor with physical CO_2 looping and 2.9 sccm (standard cubic centimeters per minute) FG10 co-feed. The *y*-axis break is added to enhance plot clarity for the low flow rate range, and only corresponds to Ar flow (grey column). Statistical data are presented as mean values with the error bars representing the standard deviations obtained from three (FE and CO_2 quantification for H_2O, *I*–*V* curves for 0.1 M $KHCO_3$) or five (all other) independent measurements.

AEM alkaline interface and its crossover to the middle chamber as carbonate, along with formate (Supplementary Notes 3 and 4 provide stoichiometry details). As protons from the anode cross the CEM into the middle chamber, one H^+ reacts with ½ CO_3^{2-}, leaving another H^+ free and forming H_2O, HCOOH and ½ CO_2.

Detected CO_2 increases to 1.52 ml min^{-1} cm^{-2} at 150 mA cm^{-2} with 0.1 M $KHCO_3$ (Fig. 2b), triple that of H_2O. pH of the middle-layer solution collected after the reaction changes from acidic (H_2O) to slightly basic when using 0.1 M $KHCO_3$ (Supplementary Fig. 6), proposing that the free H^+ react with HCO_3^- forming gas-phase CO_2. We gained further insights by deconvoluting CO_2 originating from its crossover as carbonate and its recovery from $KHCO_3$ (Supplementary Note 5). For 0.1 M $KHCO_3$, one-third of detected CO_2 originates from crossover (the only component for H_2O reactor; Supplementary Fig. 7) and two-thirds from recovery via the reaction of free H^+ and HCO_3^- (Fig. 2c). We defined CO_2 recovery efficiency as CO_2 detected on top of the

https://doi.org/10.1038/s41893-025-01755-x

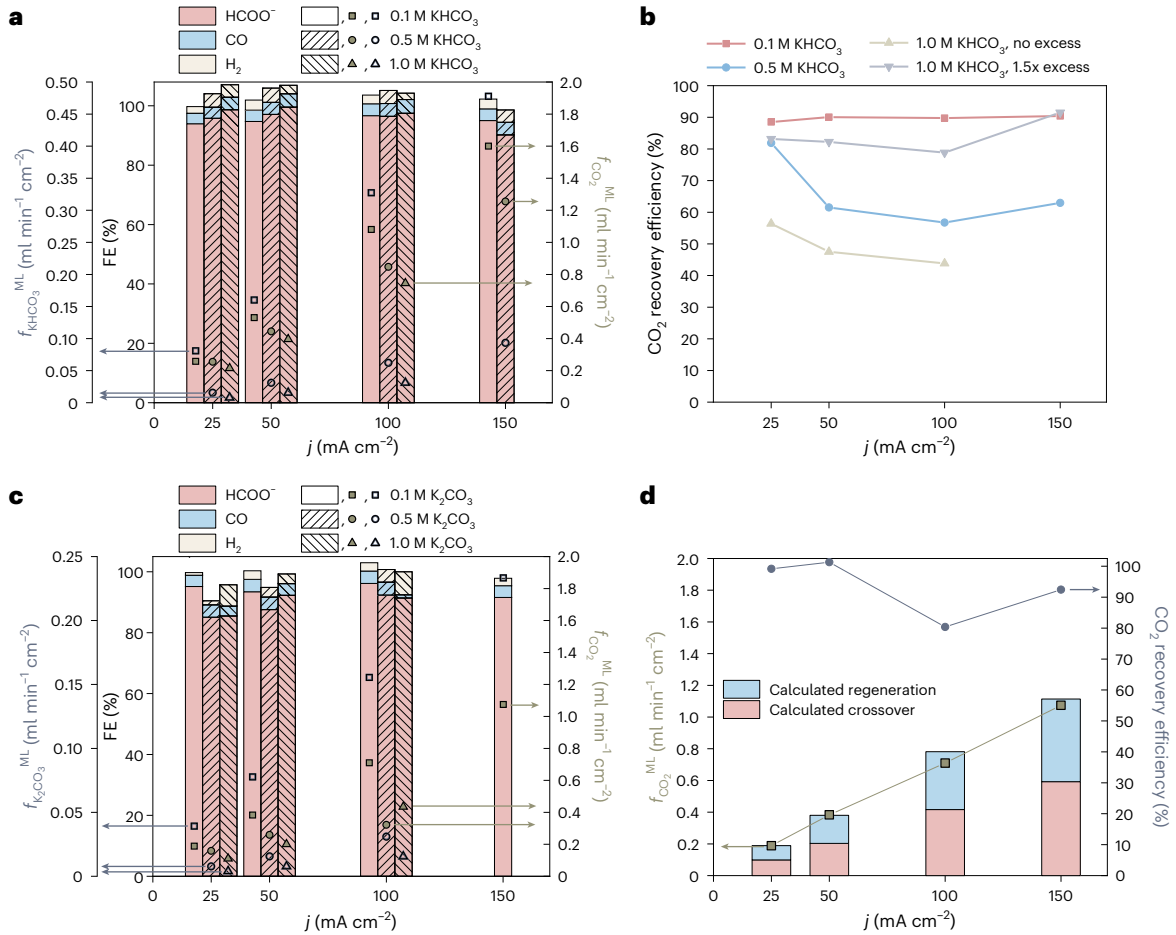

Fig. 3 | Effect of $KHCO_3$ and K_2CO_3 concentrations on CO_2 recovery process. **a**, Faradaic efficiency towards different products and CO_2 detected in the middle layer for 0.1, 0.5 and 1.0 M $KHCO_3$ middle-layer solutions. The middle-layer solution flow rates are reported as the leftmost axis, Faradaic efficiency as the primary left axis and the CO_2 detected in the outlet as the right axis. At 150 mA cm^{-2} flooding and salt build-up on the back of the GDE start to take place for 0.5 M $KHCO_3$ and completely disrupt operation for 1.0 M $KHCO_3$. **b**, CO_2 recovery efficiency in the electrolyser supplied with 0.1, 0.5, 1.0 M $KHCO_3$ with matching between the middle-layer solution flow rate and the anticipated rate of free H^+ generation and 1.0 M $KHCO_3$ supplied with 1.5× excess. **c**, Faradaic efficiency towards different products and CO_2 detected in the middle layer for 0.1, 0.5 and 1.0 M K_2CO_3 middle-layer solutions. The results indicate consistent growth of CO_2 in the middle layer for 0.1 M K_2CO_3 and slowing growth for other solutions. **d**, CO_2 detected in the middle-layer outlet, calculated values of crossover and recovered CO_2, CO_2 recovery efficiency with 0.1 M K_2CO_3 middle-layer solution supplied with matching between the middle-layer solution flow and the anticipated rate of free H^+ generation.

calculated CO_2 crossover, which we divided over the calculated recovered CO_2 amount (Supplementary Note 5 and Supplementary Fig. 8) and achieved 84–88% (Fig. 2c), evidencing high promise of the proposed concept for CO_2 recovery from 0.1 M $KHCO_3$. We highlight the possibility of CO_2 recovery from 0.1 M $NaHCO_3$ (Supplementary Fig. 9), indicating that the concept is not limited to K^+ salts. Further control tests suggest that cation conductivity difference contributes to higher resistance in the cell supplied with 0.1 M $KHCO_3$ compared to H_2O (Fig. 2a, Supplementary Fig. 10 and Supplementary Note 6).

CO_2 recovery stoichiometry depends on the applied current and FE_{HCOO^-}, which define the rate of free H^+ generation, and on the middle-layer solution flow rate and concentration. So, we switched from the fixed flow rate to the rates matched with the anticipated rate of free H^+ generation for each current density (Fig. 2d, Supplementary Tables 1 and 2 and Supplementary Note 7). Whereas FE_{HCOO^-} remains at 95% (Extended Data Fig. 1a), CO_2 recovery efficiency increases to about 90% with this approach (Fig. 2d and Extended Data Fig. 1b), HCO_3^- utilization dramatically improves to 85% (Fig. 2d) and the cell voltage decreases by about 0.3 V (Fig. 2e and Supplementary Fig. 11). Middle-layer outlet pH becomes weakly acidic (Supplementary Fig. 7), justifying higher recovery efficiency. Matching the middle-layer solution flow rate with applied current increases HCOOK concentration (Supplementary Fig. 12).

We introduced HCO_3^--to-HCOOK/$HCOO^-$ conversion efficiencies to evaluate the full bicarbonate-to-formate conversion performance. HCO_3^--to-$HCOO^-$ considers HCO_3^- utilization and FE, referring to all the formate produced in the cell. Meanwhile, HCO_3^--to-HCOOK additionally accounts for non-100% CO_2 recovery, being more restrictive and limiting the product to HCOOK. Both metrics dramatically improved with matching, reaching about 80% (Extended Data Fig. 1c) and approaching the maximum values achievable in this set-up (Supplementary Note 7 and Supplementary Fig. 13). Impedance studies (Supplementary Fig. 14 and Supplementary Note 6) indicated that lower cell voltage with the flow rate matching (Fig. 2e) is caused by accumulation of charge carriers in the middle layer and the change of primary anion from HCO_3^- to $HCOO^-$. Bubble formation is not a major contributor to the cell voltage at these conditions (Supplementary Note 6).

So far, we operated the reactor in a decoupled mode, that is, without physical supply of the recovered CO_2 to the cathode (looping; Supplementary Fig. 15) to gain fundamental insights behind CO_2 recovery and conversion. While looping is not strictly necessary for this concept viability, as CO_2 obtained in the middle chamber can

be accumulated and used to supply the cell during the next operation window, it may be more practical. So, we rewired the reactor for physical looping and successfully demonstrated 95% CO_2 recovery efficiency, 87% HCO_3^- utilization efficiency and 78% carbon-to-formate single-pass conversion efficiency without pure CO_2 supply (Fig. 2f,g, Supplementary Figs. 16–20, Extended Data Fig. 2 and Supplementary Note 8). As the absence of large differences indicates the general possibility of physical looping, we used decoupled mode for further tests to get direct access to experimental CO_2 recovery values.

Middle-layer solution variability

We have explored the effects of $KHCO_3$ concentration on the reactor performance (Figs. 2c and 3a,b, Extended Data Fig. 3a–d and Supplementary Tables 1 and 2). Notably, the amount of CO_2 generated in the middle layer decreases with the concentration increase, especially for 1.0 M $KHCO_3$ (Fig. 3a), and the middle-layer outlet turns more acidic (Supplementary Fig. 15). This indicates that although sufficient H^+ are generated, CO_2 is not recovered as a gas. For 1.0 M $KHCO_3$, salt build-up on the back of the GDE had a prominent influence on the electrolyser performance at 150 mA cm^{-2}, leading to the inability to reliably measure Faradaic efficiencies (FEs) and CO_2 flow rates.

Interestingly, we could improve the CO_2 recovery efficiency by feeding 1.0 M $KHCO_3$ at a higher flow rate compared to its stoichiometric amount, with 1.5× excess sufficient to achieve CO_2 recovery efficiency in the 75–90% range (Fig. 3b, Supplementary Figs. 21 and 22 and Extended Data Fig. 3e). As higher HCO_3^- feed rate is compensated by higher CO_2 recovery efficiency (Fig. 3b), HCO_3^- utilization efficiency does not decrease with faster flow rate and remains in the 40–55% range in both cases (Extended Data Fig. 3d). On the basis of these observations and titration control experiments (Supplementary Fig. 23), we concluded that CO_2 recovery performance decay stems from weak acidity of HCOOH, which retards the transition from bicarbonate to CO_2 in the presence of formate ions at high concentration (Supplementary Note 9). Higher $KHCO_3$ flow rate changes HCO_3^- and $HCOO^-$ ratio, helping to drive the reaction to the products according to Le Chatelier principle (Supplementary Note 9). Using a higher concentration of $KHCO_3$ middle layer brings HCOOK concentration up to 0.56 M and 4.7 wt%, compared to 0.09 M and 0.7 wt% in the 0.1 M $KHCO_3$ case (Supplementary Figs. 12 and 24), with the overall HCO_3^--to-HCOOK/$HCOO^-$ conversion efficiencies of about 50% (Extended Data Fig. 3f).

We explored whether the same reactor design can be used to recover CO_2 from K_2CO_3. As $KHCO_3$ solutions pH is close to neutral, and HCO_3^- ions cannot uptake any more CO_2, the efficiency of air contactors used as a carbon capture unit diminishes with accumulation of HCO_3^-, making CO_3^{2-} or mixed CO_3^{2-}/HCO_3^- outlets more realistic[30]. Yet, most reactive carbon capture approaches achieve optimal performance for bicarbonates, as CO_2 recovery from CO_3^{2-} is a two-step process that is hard to perform efficiently in proximity of the CO_2RR electrode[26,30,36]. Thus, the ability to use carbonate feed would greatly benefit the practicality of our design.

As CO_2 recovery and conversion occur in different parts of our electrolyser, we were able to recover CO_2 from 0.1, 0.5 and 1.0 M K_2CO_3 (Fig. 3c,d and Extended Data Fig. 4). Similar to $KHCO_3$, K_2CO_3 reactors feature lower recovery performance with concentration increase and its partial improvement when using faster flow rates. We highlight that the approach is similar to that reported in Fig. 2b,c with fixed overstoichiometric 0.1 M K_2CO_3 feed rates barely able to recover any CO_2 (Supplementary Fig. 25). We attribute this to the buffering capabilities of CO_3^{2-}/HCO_3^- solution and necessity to first convert all CO_3^{2-} to HCO_3^- and then HCO_3^- to CO_2. Thus, matching the flow rate to the anticipated $HCOO^-$ partial current and free H^+ generation rate is crucial to perform continuous CO_2 recovery from K_2CO_3. Additional insights into the operation of reactors supplied with K_2CO_3 are presented in Supplementary Figs. 26–30 and Supplementary Note 10.

Formate concentrated above bicarbonate solubility limit

To avoid the incomplete recovery of CO_2 in concentrated solutions, we have implemented the set-up in the batch configuration (Supplementary Fig. 31). Unfortunately, the salt built up too rapidly to achieve full 10 ml 1 M K_2CO_3 conversion. Still, we demonstrated that the batch set-up itself was viable at lower concentrations (Supplementary Fig. 32 and Supplementary Note 11) and proved that recovery of CO_2 from CO_3^{2-} first requires conversion to HCO_3^- and only then can proceed with CO_2 release. As the upper limit of attainable formate concentration in the three-chamber PSE reactor is fundamentally limited to $KHCO_3$ molar solubility of 3 M (20 wt%), same as in direct bicarbonate reduction electrolysers, another approach must be developed to obtain highly concentrated formate.

To achieve that, we developed a four-chamber reactor (Fig. 4a). Here we placed additional PSE layer between the AEM and original PSE chamber (further noted as PSE1) and separated it from original PSE layer (PSE2) with another CEM (Supplementary Fig. 33 and Supplementary Note 12). This modification decouples $KHCO_3$ and HCOOK and breaks the scaling relationship between their concentrations. With this, simply flowing water through the PSE1 at rates lower than $KHCO_3$ through PSE2 allows one, in principle, to obtain HCOOK of any desired concentration.

To demonstrate the validity of this concept, we used the four-chamber reactor with PSE2 supplied with 1 M $KHCO_3$ and PSE1 supplied with water at twice slower flow rate (Supplementary Fig. 34), which would ultimately yield 2 M $HCOO^-$ in PSE1. FE_{HCOO^-} remains high at about 90% (Fig. 4b), and only a minor fraction of formate is detected in PSE2 (Supplementary Fig. 35), probably due to osmotic migration of undissociated HCOOH through CEM (Supplementary Note 12). HCO_3^- utilization and CO_2 recovery from HCO_3^- in PSE2 (Supplementary Fig. 36a), identical in this cell design, were greatly improved compared to three-chamber set-up (Fig. 4c). Crossover CO_2 recovery in the PSE1 was still compromised by concentrated formate presence (Supplementary Fig. 36b), leading to complete CO_2 recovery being slightly lower than HCO_3^- utilization efficiency (Fig. 4c and Supplementary Fig. 36c) but still much higher than in the three-chamber design (Fig. 4c and Supplementary Fig. 37). The reactor produced 1.6–1.9 M $HCOO^-$ and 1.2–1.8 M HCOOK (Fig. 4d) or 9–13 wt% HCOOK (Supplementary Fig. 38). The main drawback of the four-chamber reactor is higher operating voltage (Supplementary Fig. 39); however, much better carbon balance and space for improvement justify its practicality. The use of 3 M $KHCO_3$ supply allowed us to obtain up to 5.0 M $HCOO^-$ concentration at 100 mA cm^{-2}, more than 60% higher than direct bicarbonate reduction can yield even in the ideal scenario (Fig. 4e,f, Supplementary Figs.40–44 and Supplementary Note 13).

Ethylene electrosynthesis from $KHCO_3$ as sole carbon source

Successful demonstration of the four-chamber configuration inspired us to evaluate whether the indirect bicarbonate reduction concept can be extended to other products. So far, we focused on formate as, in theory, it allows 100% HCO_3^--to-$HCOO^-$ conversion efficiency. However, typical CO_2RR reactors operate with carbon loss. Acknowledging that obtaining other products with current reactor design would be less carbon efficient, eliminating the energy-intensive CO_2 recovery step would still be valuable for the field if demonstrated with high selectivity.

We sought to elaborate whether the four-chamber reactor could produce ethylene and C_{2+} products with high selectivity. Furthermore, as CO_2RR to C_{2+} consumes less carbon atoms per electron, we decided to evaluate whether the cell can run exclusively with the 0.1 M $KHCO_3$ and no gas co-feed. Typical liquid-fed electrolysers suffer from very limited C_{2+} products selectivity due to inability to combine high alkalinity needed for C_{2+} selectivity and acidity needed for in situ CO_2 generation, the highest reported values being, to the best of our knowledge, 34% C_2H_4 and 48% C_{2+}[37].

With this, we have prepared electrode with well-studied copper nanocubes (Supplementary Fig. 45)[38,39] and performed a test

https://doi.org/10.1038/s41893-025-01755-x

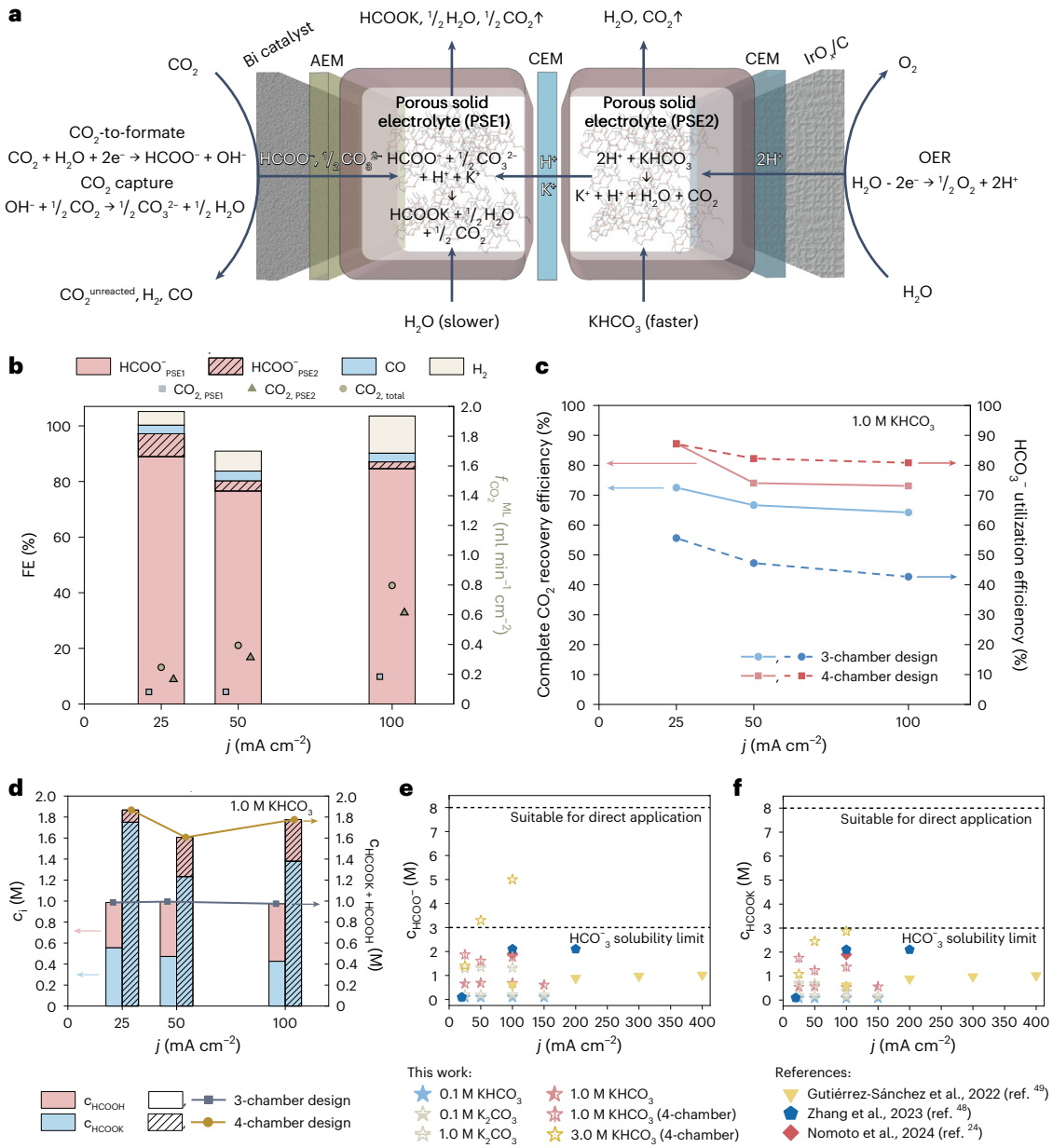

Fig. 4 | Four-chamber reactor design for electrosynthesis of concentrated HCOOK solutions. a, Illustration of the CO_2-to-formate four-chamber PSE reactor for recovery of CO_2 from $KHCO_3$ solution. This scheme highlights further separation of CO_2 recovery, which takes place in PSE2, and HCOOK collection, which takes place in PSE1. **b**, Faradaic efficiency towards different products, CO_2 detected in PSE1 and PSE2 outlets with H_2O and 1.0 M $KHCO_3$ as PSE1 and PSE2 feeding solutions. **c**, Comparison of complete CO_2 recovery and HCO_3^- utilization efficiency between the three-chamber reactor supplied with 1 M $KHCO_3$ and the four-chamber reactor supplied with H_2O (PSE1) and 1.0 M $KHCO_3$ (PSE2). The results indicate notable improvement of the carbon balance in the four-chamber reactor. **d**, Molar concentration of HCOOK, HCOOH and their cumulative concentrations in the three-chamber middle-layer solution outlet (supplied with 1.0 M $KHCO_3$) and the four-chamber reactor supplied with H_2O (PSE1) and 1.0 M $KHCO_3$ (PSE2). Our results that feeding H_2O at twice the slower rate than $KHCO_3$ nearly doubles $HCOO^-$ concentration in the product stream and increases HCOOK fraction. **e**,**f**, $HCOO^-$ and HCOOK molar concentrations obtained across this work and their comparison with the earlier works[24,48,49]. While still below market specifications, four-chamber design brings HCOOK and, especially, $HCOO^-$ concentrations much closer to the desired concentrations.

in the four-chamber cell, first in decoupled mode and then with looping (Fig. 5a). As a result, we obtained 46% C_2H_4 and 73% C_{2+} FE with the looped set-up at 150 mA cm^{-2} (Fig. 5b), featuring 12.5% HCO_3^- SPCE to C_{2+} products, high C_{2+}:C_1 products FE ratio of 9.7 (Supplementary Fig. 46a), and j_{C2H4} and j_{C2+} reaching 69 mA cm^{-2} and 106 mA cm^{-2} (Supplementary Fig. 46b). This performance is way above the current state of the art for these products selectivity in reactive carbon capture at 100+ mA cm^{-2} current densities (Fig. 5c and Supplementary Fig. 47a)[37,40–42]. This selectivity translates to a notably high share of C_2H_4 in the gas products stream, both in mass (Fig. 5d and Supplementary Fig. 47b) and, especially, in molar terms (Fig. 5d,e) due to relatively low H_2 production rates (Supplementary Fig. 46b), although higher total and partial current densities can be achieved via direct bicarbonate reduction (Supplementary Fig. 47c,d). The selectivity obtained in this work matches earlier reports for the similar nanocubes in either MEA or flow cell reactors[39,43], suggesting that any established electrode tailored for C_{2+} products formation can be translated to our indirect (bi)carbonate reduction reactor.

Deeper insight into the carbon balance indicates CO_2 recovery and HCO_3^- utilization efficiencies within 65–75% range

https://doi.org/10.1038/s41893-025-01755-x

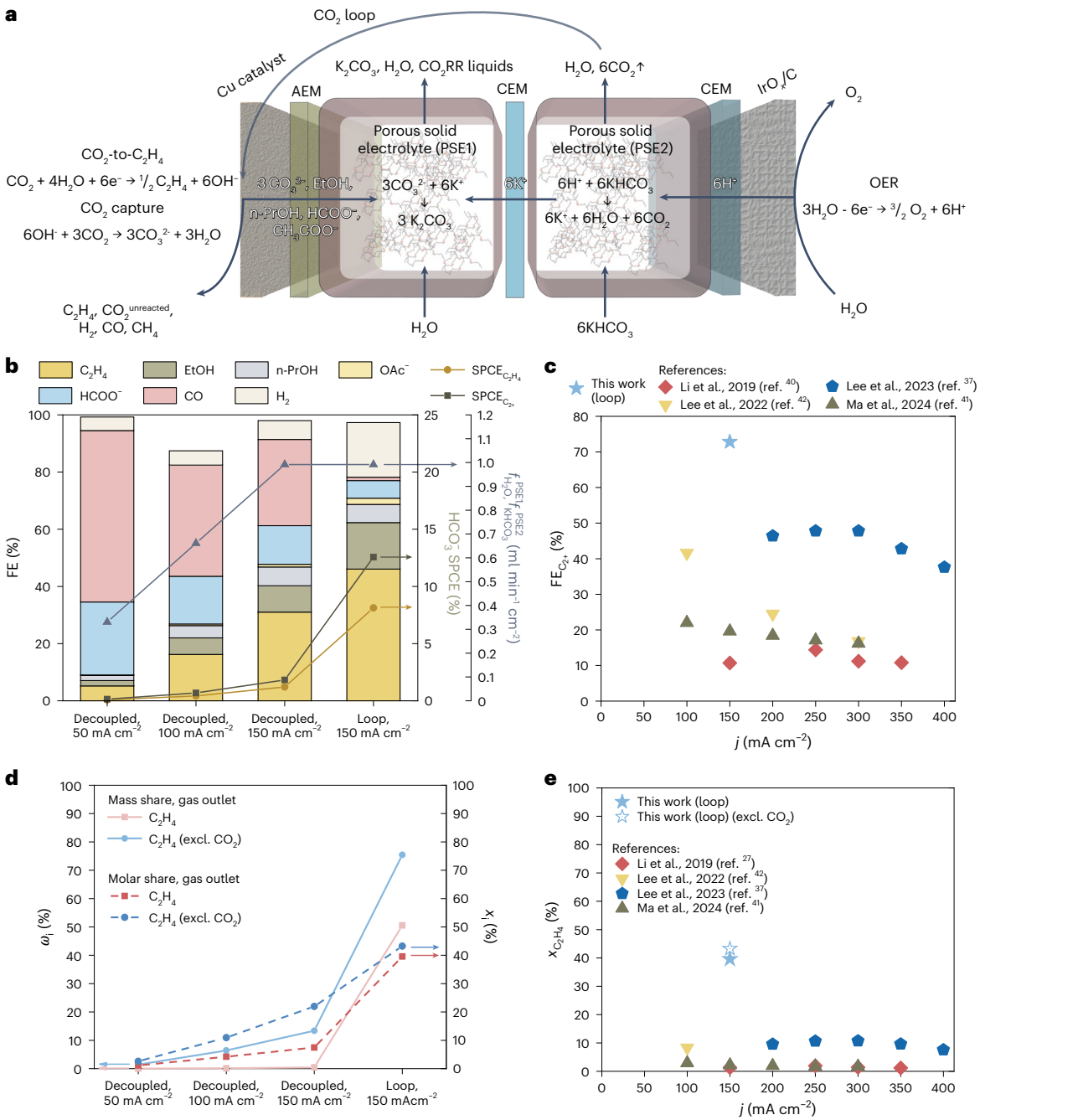

Fig. 5 | Four-chamber PSE reactor with physical loop for C_{2+} products electrosynthesis. a, Illustration of the four-chamber PSE reactor for recovery of CO_2 from $KHCO_3$ solution and its conversion for C_{2+} products via physical loop. **b**, Faradaic efficiency towards different products, HCO_3^- single-pass conversion efficiency to C_2H_4 and C_{2+} products and H_2O (PSE1) and 0.1 M $KHCO_3$ (PSE2) flow rates, equal in this case for every current density applied in both decoupled and loop configurations. The results indicate the ability of the reactor to sustain selective C_2H_4 and C_{2+} production with 0.1 M $KHCO_3$ as a sole carbon supply. **c**, Comparison of C_{2+} FE obtained in this work with previously reported results obtained with liquid-fed reactors[37,40–42]. **d**, Mass and molar shares of C_2H_4 in the cathode outlet gas stream, both including and excluding unreacted CO_2. We provided values both including and excluding CO_2 from the total outlet flow rate, as it can be removed from the stream by bubbling the outlet through alkaline solution. **e**, Comparison of the obtained molar shares of C_2H_4 including and excluding CO_2 with the previous reports[37,40–42].

(Supplementary Fig. 48). The efficiency is slightly lower for the looping compared to the decoupled operation as no gas was bubbled through the middle-layer collected solution to facilitate its collection. These efficiencies are also slightly lower than in the formate case (Supplementary Fig. 19), probably due to higher $KHCO_3$ feeding rate and higher HCO_3^-/H^+ ratio as a result. Lastly, carbon balance (Supplementary Fig. 48a) further indicates a small amount of unreacted CO_2, suggesting that the difference in selectivity profile between decoupled and looped operations arises due to much lower CO_2 flow rate and availability, in line with an earlier report[44].

Reactor stability and techno-economic analysis

We evaluated the long-term stability of the formate reactor to evaluate the practical viability of the concept. We have used decoupled mode to allow for straightforward electrolyte changes without cell CO_2 supply interruptions and direct results quantification. At 100 mA cm^{-2} applied

https://doi.org/10.1038/s41893-025-01755-x

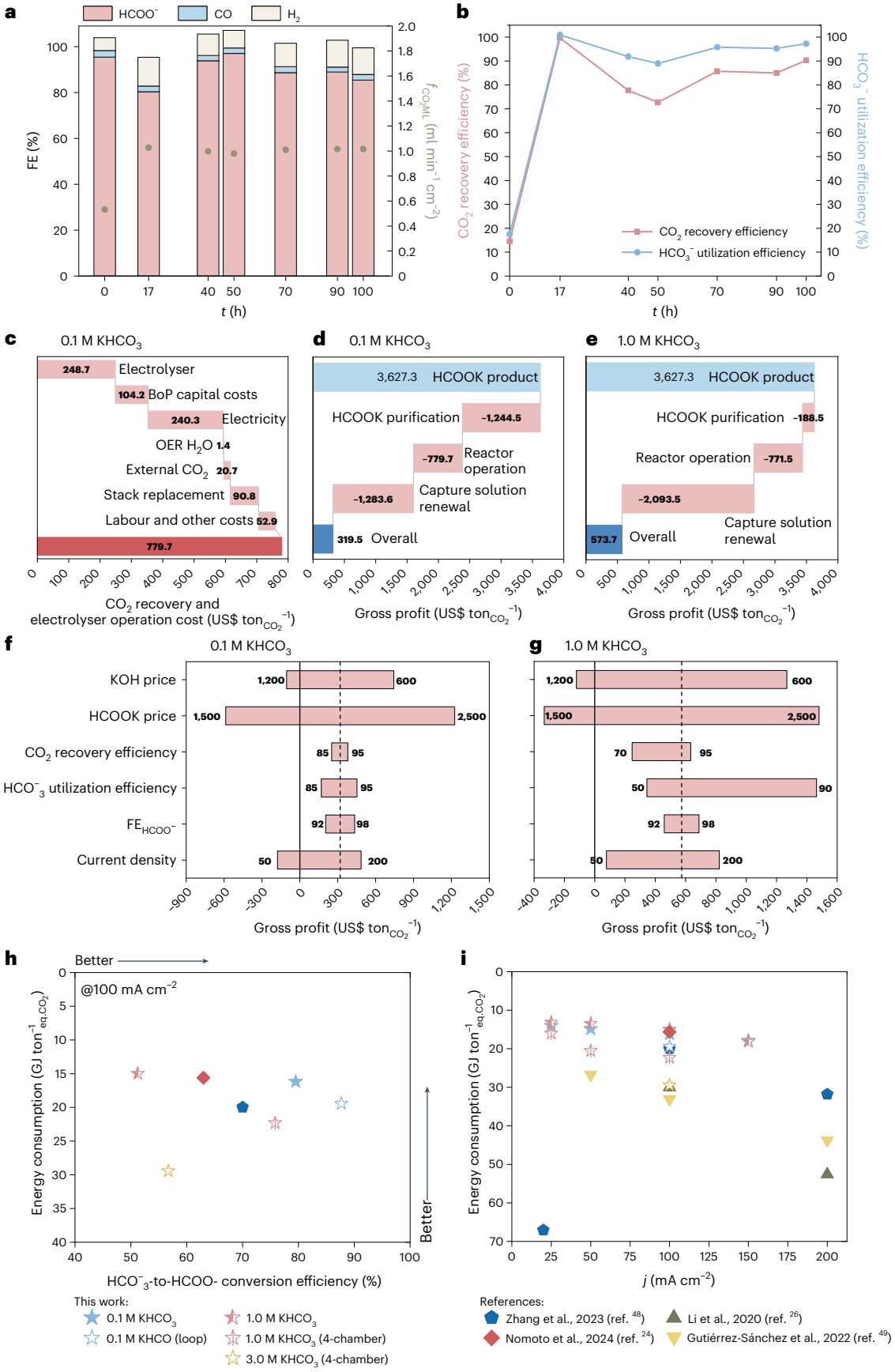

Fig. 6 | Reactor stability, its TEA metrics and energy consumption. **a**,**b**, Faradaic efficiencies and CO_2 detected in the middle layer (**a**) and CO_2 recovery and HCO_3^- utilization efficiencies for 0.1 M $KHCO_3$ middle-layer solution during CO_2RR for 100 h at 100 mA cm^{-2} (**b**). These results indicate reasonably stable CO_2 recovery process for up to 100 h. **c**,**d**, TEA of our single-unit CO_2 recovery and conversion reactor supplied with 0.1 M $KHCO_3$ solution: operation costs (**c**), overall process profitability (**d**). **e**, Overall process profitability of our three-chamber CO_2 recovery and conversion reactor supplied with 1.0 M $KHCO_3$ solution. **f**,**g**, Sensitivity analysis of the process profitability as a function of key variables (KOH and HCOOK costs, CO_2 recovery and HCO_3^- conversion efficiencies, FE_{HCOO^-}, current density). 1.0 M $KHCO_3$ supply provides more robust TEA metrics due to lowered product separation costs, with most scenarios staying in the profitable region. **h**,**i**, Comparison of the overall HCO_3^--to-$HCOO^-$ process energy consumption between our studies and state-of-the-art approaches normalized by 1 ton_{CO2} plotted as functions of (H) HCO_3^--to-$HCOO^-$ conversion efficiency (at 100 mA cm^{-2}) (**h**) and current density[24,26,48,49] (**i**). Overall, this comparison suggests that our approach can offer highly competitive HCO_3^--to-formate energy needed for CO_2 recovery from the carbon capture solutions and its conversion to the formate with state-of-the-art carbon efficiency.

current density with 0.1 M $KHCO_3$, the reactor maintains 85–90% CO_2 recovery efficiency for about 30 h, after which it rapidly deteriorates (Supplementary Fig. 49). Interestingly, we could extend the lifetime three times by intentionally 'underpacking' the middle chamber with ion-exchange resin beads to decrease the volume fraction occupied by the solid in the middle layer and allow more space for the gas (Supplementary Notes 2 and 14). This assembly maintained about 90% FE_{HCOO^-} and about 85% CO_2 recovery efficiency for 100 h (Fig. 6a,b and Supplementary Fig. 50) at the cost of slightly higher cell voltage due to lower middle-layer conductivity (Supplementary Fig. 51). The similarity between the failure modes of the cell during extended operation with 0.1 M $KHCO_3$, short-term operation with concentrated solutions and at high currents suggest that the strategies to mitigate the failures will probably be the same; we present their brief overview in Supplementary Note 2.

With plenty of room for further optimization, operational stability of our electrolyser indicates practical promise, and we evaluated its potential from the techno-economic analysis (TEA) perspective (Supplementary Note 15 and Supplementary Tables 4–11). While it may appear detrimental that our set-up produces HCOOK rather than HCOOH, they share different markets with distinct applications. Featuring high value as a sustainable drilling, deicing, heat transfer, textile dyeing and leather tanning liquid, HCOOK has slightly higher market size compared to HCOOH (about US$0.8 billion in 2024 growing to US$1.1 billion in 2032 for HCOOK, compared to US$0.7 billion in 2024 growing to US$0.9 billion in 2032 for HCOOH), justifying its production relevance and no need for its conversion to HCOOH[45–47].

We evaluated the reactor operation costs, process profitability and performed sensitivity analysis for every representative design we used (Supplementary Notes 15 and 16). The process is profitable using 0.1 M $KHCO_3$ at 100 mA cm^{-2} both in decoupled mode (Fig. 6c,d, Supplementary Fig. 53 and Supplementary Table 4) and with looping (Supplementary Fig. 54 and Supplementary Table 5). However, the necessity to concentrate the obtained HCOOK decreases the overall profitability with 0.1 M $KHCO_3$ (Fig. 6d and Supplementary Fig. 54b) compared to 1.0 M $KHCO_3$, which provides better metrics, both in the three-chamber (US$573.7 ton^{-1}_{CO2} profit, 16% profit margin; Fig. 6e, Supplementary Fig. 55 and Supplementary Table 6) and four-chamber configurations (Supplementary Fig. 56 and Supplementary Table 7). Currently, transition to 3.0 M $KHCO_3$ leads to worse metrics due to poorer electrochemical performance (Supplementary Fig. 57 and Supplementary Table 8). 0.1 M K_2CO_3 is profitable thanks to its high electrochemical performance (Supplementary Fig. 58 and Supplementary Table 9), but 1.0 M K_2CO_3 is not profitable in the three-chamber reactor due to the trade-offs between CO_2 recovery and CO_3^{2-} utilization (Supplementary Fig. 59 and Supplementary Table 10). Sensitivity analysis indicates the highest sensitivity of all scenarios to HCOOK cost and FE_{HCOO^-}, followed by CO_2 recovery, HCO_3^-/CO_3^{2-} utilization, KOH cost and, for diluted solutions, H_2O removal (HCOOK purification) (Fig. 6f,g, Supplementary Tables 4–10 and Supplementary Fig. 53–59).

Compared to direct bicarbonate reduction[24,26,48,49], our process offers comparable energy consumption[8] but better carbon utilization despite operating in the single-pass configuration (Fig. 6h,i, Supplementary Fig. 60 and Supplementary Notes 17 and 18). We have presented the data based on the HCO_3^--to-$HCOO^-$ conversion in Fig. 6h,i (16–20 GJ ton^{-1}_{CO2}), as the reference reports do not discuss the formate speciation; the plot based on HCO_3^--to-HCOOK conversion is also reported (Supplementary Fig. 61, yielding 18–22 GJ ton^{-1}_{CO2}). We did not include the results obtained for K_2CO_3 due to the energy calculation ambiguity (Supplementary Note 17); however, the approaches used for comparison are generally unable to utilize carbonate supply[24,26,48,49]

Discussion

We designed an electrochemical reactor that performs single-unit CO_2 recovery and conversion without the need to use separate, costly annealing to recover CO_2 from the capture solutions. Our approach combines the benefits of reactive carbon capture, which improves the overall energy efficiency and economic parameters of the electrolyser, and sequential CO_2 recovery and conversion, which allows to independently tune each process in the electrolyser and push its efficiency. The modular and versatile nature of the proposed concept ensured compatibility with various upstream and downstream processes, streamlining its potential practical implementation. Our work calls for further studies aimed at addressing cathode flooding and salt build-up, which are major stability limitations, and targeting larger reactors to obtain highly concentrated liquid product to further improve the proposed concept and close the gap to the real application.

Methods

Chemicals

$KHCO_3$ (puriss., meets analytical specification of Ph. Eur., BP, USP, E501, 99.5–101.0% (acidimetric) or ACS reagent 99.7%, granular), K_2CO_3 (ACS reagent, ≥ 99.0%), $NaHCO_3$ (ACS reagent, ≥ 99.0%), 200–400 mesh DOWEX cation-exchange resin and Nafion 117 ionomer (5% in a mixture of lower aliphatic alcohols and water) were acquired from Sigma Aldrich. Deuterium oxide (99.9%) was acquired from Cambridge Isotope Laboratories Inc. Bi_2O_3 nanoparticles (99.9%, 80 nm) were purchased from US Research Nanomaterials Inc. All chemicals were used without further purification.

Working electrode preparation

To prepare the Bi_2O_3-coated working cathode of 1.5 × 1.5 cm^2, we first prepared the ink containing 60 mg of Bi_2O_3 nanoparticles, 240 µl of the Nafion 117 binder and 6 ml of isopropanol and sonicated the ink for 30 minutes. Then, we sprayed the ink with the airbrush onto the 6 × 6 cm^2 gas diffusion electrode (Sigracet 39BB, Fuel cell store) on a hotplate at 50 °C. The balance was used to weigh the electrode before and after spraying to ensure the consistent loading of 1 mg cm^{-2} of Bi_2O_3 on the GDE. Finally, the 1.5 × 1.5 cm^2 piece was cut from the sprayed GDE piece to run electrochemical tests.

To prepare the Cu nanocubes electrode, the same Sigracet 39BB gas diffusion electrode was used. The nanocubes were synthesized according to the previously reported procedure and come as colloidal solutions in toluene[38]. To remove native organic ligands before spraying, we performed solvent washing by adding 1:1 volume of ethanol to the colloidal solution containing the nanocubes and centrifuged them for 10 min at 11,510 rcf (relative centrifugal force). After that, the supernatant was discarded, THF was added to redisperse the ligand-free

nanocubes, and the solution was sprayed using the airbrush onto the gas diffusion electrode to obtain the loading of 0.25 mg cm^{-2}.

Transmission electron microscopy (TEM) images of Cu nanocubes were acquired on a Thermo-Fisher Tecnai-Spirit at 120 kV. Ten microlitres of as-synthesized NPs were drop-cast on a carbon-coated copper TEM grid (Ted Pella) to prepare the sample for imaging.

Electrochemical CO_2 reduction

All electrochemical measurements were performed using a Bio-Logic VMP3 workstation and EC-Lab software. For the porous solid electrolyte (PSE) assembly, a stainless-steel endplate was used as a cathode plate, titanium plate was used as an anode plate, and polycarbonate plastic compartment was used as a middle layer. The prepared Bi_2O_3 on the GDE was used as a cathode with a PTFE gasket that ensures ~20% compression on the GDE. The middle layer was packed with a 200–400 mesh DOWEX cation-exchange resin, and the commercial IrO_2 anode (Dioxide Materials)[33] was used for the OER reaction. CO_2 (pure clean, 99.995%, Airgas) was flowed through the bubbler into the cathode back channel using an Alicat Scientific mass flow controller for the tests in decoupled mode; for the tests with physical looping, the middle layer collection flask outlet, either with or without 10% CO_2 flue gas (balanced with 90% Ar, Airgas), was directly supplied to the cathode. The liquid level in the collection flask was kept constant by constant draining of liquid at the same rate as middle-layer solution flow rate supply to avoid pushing the CO_2 to the cathode in amounts larger than electrochemically recovered. For the stability tests, the bubbler was heated to 45 °C to minimize the salt formation on the back of the GDE. The middle chamber was fed by solution of choice (Milli-Q water, $KHCO_3$ or K_2CO_3) using the peristaltic pump or the syringe pump for the rates higher or lower than 0.1 ml min^{-1}, respectively. The middle-layer solution was allowed to flow through the cell for 30 min before the beginning of the experiment. A Nafion 117 cation-exchange membrane (CEM) was placed between the middle layer and the anode, and a 40-µm-thick PiperION (Versogen) anion-exchange membrane (AEM) was placed between the middle layer and the cathode. All electrolyser tests in this study were based on a 2.25 cm^2 electrode area, and no ohmic loss compensation was applied.

We analysed the gas products formed during the CO_2RR (H_2 and CO) with SRI 8610 C or Shimadzu GC-2014 gas chromatograph. We have used a traditional soap film flowmeter to measure the cathode gas outlet flow rate to allow reliable Faradaic efficiency calculations of the gas products. To quantify the amount of formate formed during reaction, we have used nuclear magnetic resonance Bruker AV III HD 500 MHz spectrometer with an internal standard of dimethyl sulfoxide/deuterium oxide. Finally, we quantified the amount of CO_2 in the middle layer by mixing its outlet with an inert gas (Ar, ultra-high purity, 99.9999%, Airgas), allowing to separate liquid and gas phases in the collecting flask and feeding the gas stream into a CO_2 sensor (CO2Meter, Gaslab). To ensure that all detected CO_2 originates from either crossover or CO_2 recovery at a given current density, we have disposed of the collected liquid after every current density change, purged the middle-layer solutions with inert gas for 30 min before measurements and kept Ar flowing over the surface during the operation. In all cases, we have performed the measurements only after the voltage and CO_2 sensor reading were stabilized. The error bars represent the standard deviations obtained over the course of at least three independent measurements.

Reporting summary

Further information on research design is available in the Nature Portfolio Reporting Summary linked to this article.

Data availability

Data supporting the findings of this Article are available in the Supplementary Information. Source data are provided with this paper.

References

1. IPCC *Climate Change 2022: Mitigation of Climate Change* (eds Shukla, P. R. et al.) (Cambridge Univ. Press, 2022); https://doi.org/10.1017/9781009157926
2. Gao, W. et al. Industrial carbon dioxide capture and utilization: state of the art and future challenges. *Chem. Soc. Rev.* **49**, 8584–8686 (2020).
3. Sullivan, I. et al. Coupling electrochemical CO_2 conversion with CO_2 capture. *Nat. Catal.* **4**, 952–958 (2021).
4. Li, M., Irtem, E., Iglesias van Montfort, H. P., Abdinejad, M. & Burdyny, T. Energy comparison of sequential and integrated CO_2 capture and electrochemical conversion. *Nat. Commun.* **13**, 5398 (2022).
5. Sanz-Pérez, E. S., Murdock, C. R., Didas, S. A. & Jones, C. W. Direct capture of CO_2 from ambient air. *Chem. Rev.* **116**, 11840–11876 (2016).
6. Chatterjee, S. & Huang, K. W. Unrealistic energy and materials requirement for direct air capture in deep mitigation pathways. *Nat. Commun.* **11**, 3287 (2020).
7. Eisaman, M. D., Alvarado, L., Larner, D., Wang, P. & Littau, K. A. CO_2 desorption using high-pressure bipolar membrane electrodialysis. *Energy Environ. Sci.* **4**, 4031–4037 (2011).
8. Zhang, X., Fang, Z., Zhu, P., Xia, Y. & Wang, H. Electrochemical regeneration of high-purity CO_2 from (bi)carbonates in a porous solid electrolyte reactor for efficient carbon capture. *Nat. Energy* **10**, 55–65 (2025).
9. Digdaya, I. A. et al. A direct coupled electrochemical system for capture and conversion of CO_2 from oceanwater. *Nat. Commun.* **11**, 4412 (2020).
10. Muroyama, A. P. & Gubler, L. Carbonate regeneration using a membrane electrochemical cell for efficient CO_2 capture. *ACS Sustain. Chem. Eng.* **10**, 16113–16117 (2022).
11. Shu, Q., Legrand, L., Kuntke, P., Tedesco, M. & Hamelers, H. V. M. Electrochemical regeneration of spent alkaline absorbent from direct air capture. *Environ. Sci. Technol.* **54**, 8990–8998 (2020).
12. Vallejo Castaño, S. et al. Optimizing alkaline solvent regeneration through bipolar membrane electrodialysis for carbon capture. *Chem. Eng. J.* **488**, 150870 (2024).
13. Freyman, M. C. et al. Reactive CO_2 capture: a path forward for process integration in carbon management. *Joule* **7**, 631–651 (2023).
14. Siegel, R. E., Pattanayak, S. & Berben, L. A. Reactive capture of CO_2: opportunities and Challenges. *ACS Catal.* **13**, 766–784 (2023).
15. Dongare, S. et al. Reactive capture and electrochemical conversion of CO_2 with ionic liquids and deep eutectic solvents. *Chem. Soc. Rev.* **53**, 8563–8631 (2024).
16. Bruggeman, D. F., Rothenberg, G. & Garcia, A. C. Investigating proton shuttling and electrochemical mechanisms of amines in integrated CO_2 capture and utilization. *Nat. Commun.* **15**, 9207 (2024).
17. Chen, L. et al. Electrochemical reduction of carbon dioxide in a monoethanolamine capture medium. *ChemSusChem* **10**, 4109–4118 (2017).
18. Pérez-Gallent, E., Vankani, C., Sánchez-Martínez, C., Anastasopol, A. & Goetheer, E. Integrating CO_2 capture with electrochemical conversion using amine-based capture solvents as electrolytes. *Ind. Eng. Chem. Res.* **60**, 4269–4278 (2021).
19. Zhang, Z. et al. Porous metal electrodes enable efficient electrolysis of carbon capture solutions. *Energy Environ. Sci.* **15**, 705–713 (2022).
20. Lee, G. et al. Electrochemical upgrade of CO_2 from amine capture solution. *Nat. Energy* **6**, 46–53 (2020).
21. Xiao, Y. C. et al. Reactive capture of CO_2 via amino acid. *Nat. Commun.* **15**, 7849 (2024).

22. Jewlal, A. M. L., Kim, Y., Crescenzo, G. V. & Berlinguette, C. P. Go with CO: a case for targeting carbon monoxide as a reactive carbon capture product. *ACS Energy Lett.* **10**, 2498–2502 (2025).
23. Kim, Y. et al. Integrated CO_2 capture and conversion to form syngas. *Joule* **8**, 3106–3125 (2024).
24. Nomoto, K., Okazaki, T., Beppu, K., Shishido, T. & Amano, F. Highly selective formate formation via bicarbonate conversions. *EES Catal.* **2**, 1277–1284 (2024).
25. Carneiro, J. S. A. et al. Insights into the oxidative degradation mechanism of solid amine sorbents for CO_2 capture from air: roles of atmospheric water. *Angew. Chem. Int. Ed.* **62**, e202302887 (2023).
26. Li, T., Lees, E. W., Zhang, Z. & Berlinguette, C. P. Conversion of bicarbonate to formate in an electrochemical flow reactor. *ACS Energy Lett.* **5**, 2624–2630 (2020).
27. Li, T. et al. Electrolytic conversion of bicarbonate into CO in a flow cell. *Joule* **3**, 1487–1497 (2019).
28. Song, H. et al. Integrated carbon capture and CO production from bicarbonates through bipolar membrane electrolysis. *Energy Environ. Sci.* **17**, 3570–3579 (2024).
29. Keith, D. W., Holmes, G., St. Angelo, D. & Heidel, K. A process for capturing CO_2 from the atmosphere. *Joule* **2**, 1573–1594 (2018).
30. Almajed, H. M. et al. Closing the loop: unexamined performance trade-offs of integrating direct air capture with (bi)carbonate electrolysis. *ACS Energy Lett.* **9**, 2472–2483 (2024).
31. Nankya, R., Elgazzar, A., Zhu, P., Chen, F. Y. & Wang, H. Catalyst design and reactor engineering for electrochemical CO_2 reduction to formate and formic acid. *Mater. Today* **76**, 94–109 (2024).
32. Kim, J. Y.'Timothy' et al. Recovering carbon losses in CO_2 electrolysis using a solid electrolyte reactor. *Nat. Catal.* **5**, 288–299 (2022).
33. Kutz, R. B. et al. Sustainion imidazolium-functionalized polymers for carbon dioxide electrolysis. *Energy Technol.* **5**, 929–936 (2017).
34. Elgazzar, A. et al. Electrochemical CO_2 reduction to formic acid with high carbon efficiency. *ACS Energy Lett.* **10**, 450–458 (2024).
35. Fan, L., Xia, C., Zhu, P., Lu, Y. & Wang, H. Electrochemical CO_2 reduction to high-concentration pure formic acid solutions in an all-solid-state reactor. *Nat. Commun.* **11**, 3633 (2020).
36. Namdari, M., Kim, Y., Pimlott, D. J. D., Jewlal, A. M. L. & Berlinguette, C. P. Reactive carbon capture using electrochemical reactors. *Chem. Soc. Rev.* **54**, 590–600 (2025).
37. Lee, G. et al. CO_2 electroreduction to multicarbon products from carbonate capture liquid. *Joule* **7**, 1277–1288 (2023).
38. Loiudice, A. et al. Tailoring copper nanocrystals towards C_2 products in electrochemical CO_2 reduction. *Angew. Chem. Int. Ed.* **55**, 5789–5792 (2016).
39. Larrazábal, G. O., Okatenko, V., Chorkendorff, I., Buonsanti, R. & Seger, B. Investigation of ethylene and propylene production from CO_2 reduction over copper nanocubes in an MEA-type electrolyzer. *ACS Appl. Mater. Interfaces* **14**, 7779–7787 (2022).
40. Li, Y. C. et al. CO_2 electroreduction from carbonate electrolyte. *ACS Energy Lett.* **4**, 1427–1431 (2019).
41. Ma, S. et al. Cathode surface pH modulates multicarbon product selectivity during the electrochemical conversion of CO_2 capture solutions. *ACS Energy Lett.* **9**, 2326–2332 (2024).
42. Lee, J., Liu, H. & Li, W. Bicarbonate electroreduction to multicarbon products enabled by Cu/Ag bilayer electrodes and tailored microenviroments. *ChemSusChem* **15**, e202201329 (2022).
43. De Gregorio, G. L. et al. Facet-dependent selectivity of Cu catalysts in electrochemical CO_2 reduction at commercially viable current densities. *ACS Catal.* **10**, 4854–4862 (2020).
44. Tan, Y. C., Lee, K. B., Song, H. & Oh, J. Modulating local CO_2 concentration as a general strategy for enhancing C–C coupling in CO_2 electroreduction. *Joule* **4**, 1104–1120 (2020).
45. Liu, S. et al. Potassium formate-based electrolytes for high performance aqueous electrochemical capacitors. *J. Power Sources* **541**, 231657 (2022).
46. Potassium formate market size, share & industry analysis by form (liquid and solid), by application (oil & gas, de-icing, heat transfer fluids, and others), and regional forecast, 2024-2032. *Fortune Business Insights* https://www.fortunebusinessinsights.com/potassium-formate-market-109687 (2023).
47. Formic acid market size, share & industry analysis, by grade (85%, 94%, 99%, and others), by application (agriculture, leather & textile, chemical, rubber, pharmaceuticals, and others), and regional forecast, 2025-2032. *Fortune Business Insights* https://www.fortunebusinessinsights.com/formic-acid-market-104888 (2024).
48. Zhang, Z., Xi, D., Ren, Z. & Li, J. A carbon-efficient bicarbonate electrolyzer. *Cell Rep. Phys. Sci.* **4**, 101662 (2023).
49. Gutiérrez-Sánchez, O., De Mot, B., Bulut, M., Pant, D. & Breugelmans, T. Engineering aspects for the design of a bicarbonate zero-gap flow electrolyzer for the conversion of CO_2 to formate. *ACS Appl. Mater. Interfaces* **14**, 30760–30771 (2022).

Acknowledgements

V.O., A.E. and H.W. acknowledge the support from the Robert A. Welch Foundation (grant number C-2051-20230405) and the David and Lucile Packard Foundation (grant number 2020-71371).

Author contributions

H.W. supervised the project. V.O. performed the tests and related data processing. A.E. assisted with electrochemical tests. A.L. synthesized copper nanocubes and performed their TEM. V.O. wrote the manuscript. H.W. revised the manuscript. V.O., H.W., A.E., A.L. and R.B. discussed the results and provided comments on the manuscript.

Competing interests

The authors declare no competing interests.

Additional information

Extended data is available for this paper at https://doi.org/10.1038/s41893-025-01755-x.

Supplementary information The online version contains supplementary material available at https://doi.org/10.1038/s41893-025-01755-x.

Correspondence and requests for materials should be addressed to Haotian Wang.

Peer review information *Nature Sustainability* thanks Ung Lee, Hongyan Liang and Mahinder Ramdin for their contribution to the peer review of this work.

https://doi.org/10.1038/s41893-025-01755-x

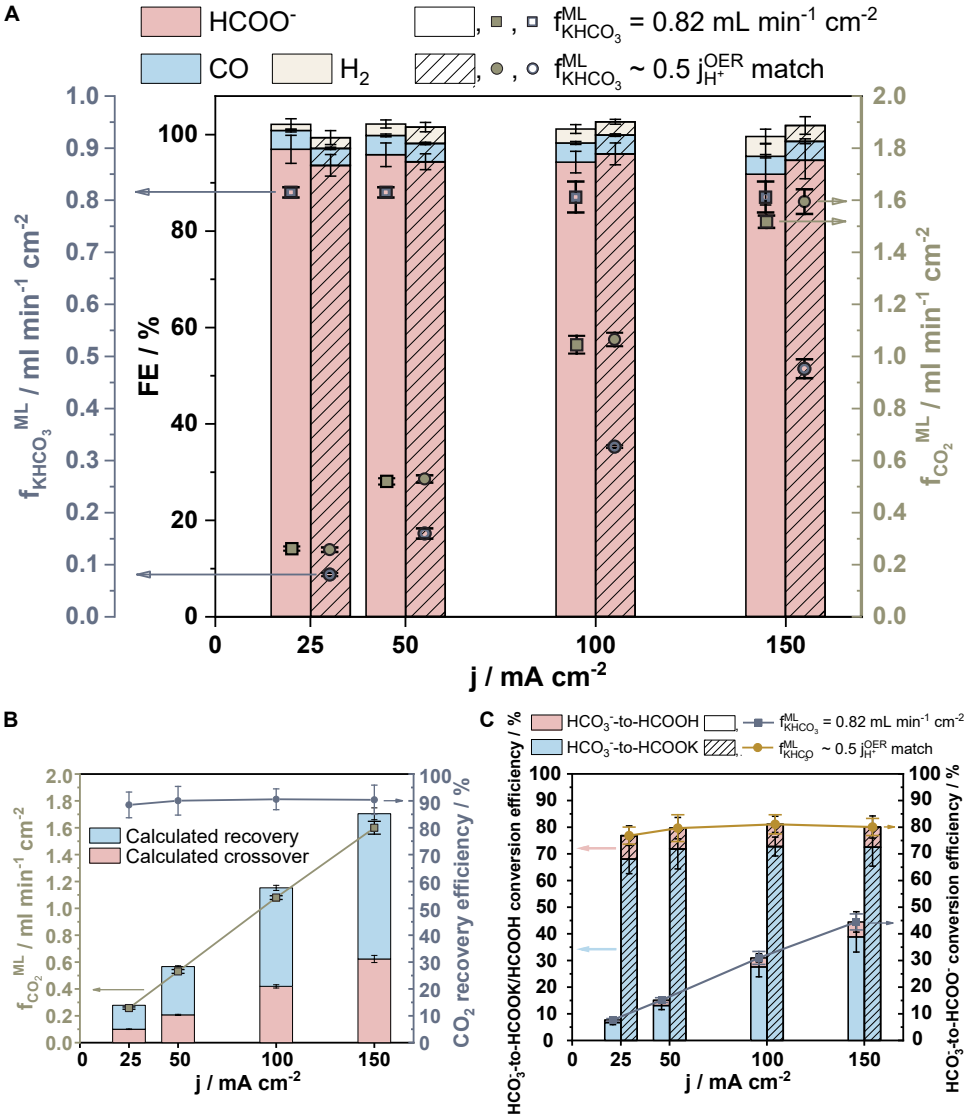

Extended Data Fig. 1 | Role of the middle-layer solution on reaction stoichiometry, CO_2 recovery and HCO_3^--to-$HCOO^-$ conversion. (**A**) Faradaic efficiencies and CO_2 detected in the middle-layer fed at fixed rate of 0.82 ml min^{-1} cm^{-2} (or 1.85 ml min^{-1}) and with matching between the middle-layer solution flow rate and the anticipated rate of free H^+ generation (molar equivalent of 0.5 $j_{H^+}^{OER}$). The middle-layer solution flow rates are reported as the leftmost axis, Faradaic efficiency as the primary left axis, and the CO_2 detected in the outlet as the right axis. Comparable FE_{HCOO^-} is observed in both cases, while CO_2 detected in the middle-layer solution is higher with matching. (**B**) CO_2 detected in the middle-layer outlet, calculated crossover and recovered CO_2 values, and CO_2 recovery efficiency with 0.1 M $KHCO_3$ as middle-layer solution with matching between its flow rate and the anticipated rate of free H^+ generation, indicating consistent CO_2 recovery efficiency of about 90%. (C) HCO_3^--to-HCOOK, HCOOH and $HCOO^-$ (combined) conversion efficiencies in our single-unit CO_2 recovery and conversion electrolyser with 0.1 M $KHCO_3$ middle-layer solution with a fixed rate and with matching between its flow rate and the anticipated rate of free H^+ generation. HCO_3^--to-HCOOK conversion efficiency is the most restrictive metric used in our study, as it accounts for non-100% HCO_3^- utilization, Faradaic and CO_2 recovery. Data are presented as mean values, with the error bars representing the standard deviations obtained from five independent measurements.

https://doi.org/10.1038/s41893-025-01755-x

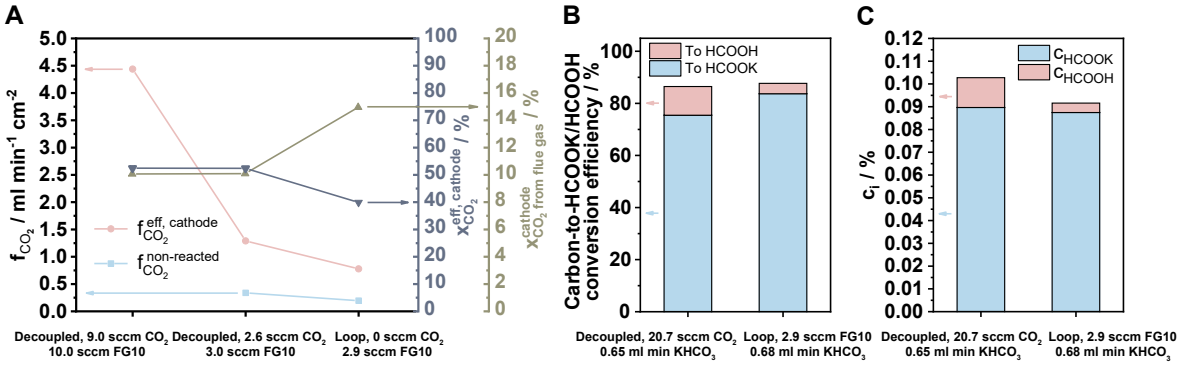

Extended Data Fig. 2 | Reactor performance with physical looping of recovered CO_2 to the cathode. (**A**) Comparison of effective CO_2 concentrations and flow rates at the cathode, unreacted CO_2 and share of CO_2 originating from FG10 in the overall CO_2 supply to the cathode. (**B**) Bicarbonate and flue gas to $HCOO^-$, HCOOH and HCOOK conversion efficiencies and (**C**) molar $HCOO^-$, HCOOH and HCOOK concentrations in the reactor operated at 100 mA cm^{-2} supplied with 20.7 sccm CO_2 (cathode) and 0.1 M $KHCO_3$ at flow rate of 0.65 ml min^{-1} (PSE layer) in decoupled mode, and with 0.1 M $KHCO_3$ at flow rate of 0.68 ml min^{-1} and 2.9 sccm FG10 co-feed (looped).

https://doi.org/10.1038/s41893-025-01755-x

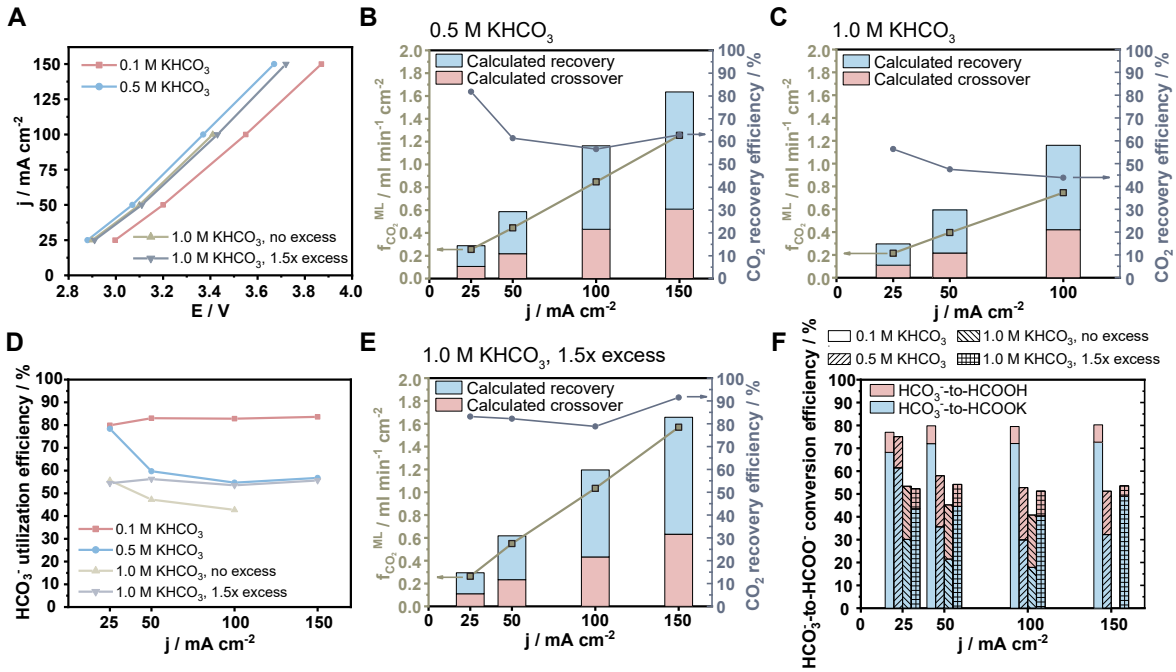

Extended Data Fig. 3 | Detailed performance of CO_2 recovery and conversion reactor supplied with $KHCO_3$ solutions of different concentrations. (**A**) The I-V curves of the CO_2-to-formate PSE reactor with 0.1, 0.5 and 1.0 M $KHCO_3$ middle-layer solutions and matching between the middle-layer solution flow rate and the anticipated rate of free H^+ generation, as well as with 1.0 M $KHCO_3$ supplied at 1.5× excess compared to the anticipated stoichiometric amount. The results indicate only minor differences in these four scenarios. (**B**, **C**) CO_2 detected in the middle-layer outlet, calculated values of crossover and recovered CO_2, and CO_2 recovery efficiency with (**B**) 0.5 M $KHCO_3$ and (**C**) 1.0 M $KHCO_3$ as middle-layer solutions. (**D**) HCO_3^- utilization efficiency in our single-unit CO_2 recovery and conversion electrolyser supplied with 0.1, 0.5, 1.0 M $KHCO_3$ with matching between the middle-layer solution flow rate and the anticipated rate of free H^+ generation, as well as 1.0 M $KHCO_3$ supplied with 1.5× excess compared to its stoichiometric flow rate. (**E**) CO_2 detected in the middle-layer outlet, calculated values of crossover and recovered CO_2, and CO_2 recovery efficiency with 1.0 M $KHCO_3$ middle-layer solution supplied with 1.5× excess compared to anticipated stochiometric amount. (**F**) HCO_3^--to-HCOOK, HCO_3^--to-HCOOH and HCO_3^--to-$HCOO^-$ (combined) conversion efficiencies in our electrolyser supplied with 0.1, 0.5, 1.0 M $KHCO_3$ with matching between the middle-layer solution flow rate and the anticipated rate of free H^+ generation, as well as 1.0 M $KHCO_3$ supplied with 1.5× excess compared to its stoichiometric flow rate.

https://doi.org/10.1038/s41893-025-01755-x

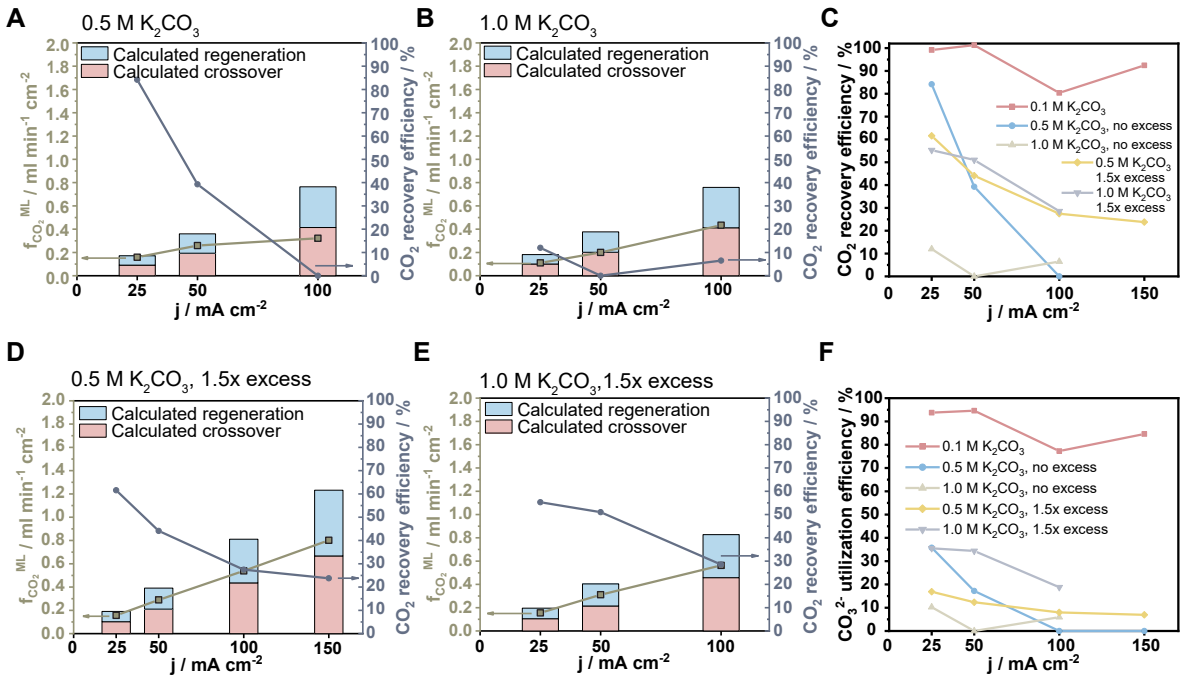

Extended Data Fig. 4 | Detailed performance of CO_2 recovery and conversion reactor supplied with K_2CO_3 solutions of different concentrations. (**A**, **B**) CO_2 detected in the middle-layer outlet, calculated values of crossover and recovered CO_2, and CO_2 recovery efficiency with (**A**) 0.5 and (**B**) 1.0 M K_2CO_3 as middle-layer solutions with matching between the middle-layer solution flow rate and the anticipated rate of free H^+ generation. (**C**) CO_2 recovery efficiencies for different K_2CO_3 middle layer solutions. Supplying excess K_2CO_3 helps to retain higher CO_2 recovery efficiency for 0.5 M and 1.0 M K_2CO_3, particularly at current densities higher than 50 mA cm^{-2}. (**D**, **E**) CO_2 detected in the middle-layer outlet, calculated values of crossover and recovered CO_2, and CO_2 recovery efficiency with (**D**) 0.5 and (**E**) 1.0 M K_2CO_3 fed as middle-layer solutions supplied at 1.5× excess. (**F**) CO_3^{2-} recovery efficiencies for different K_2CO_3 middle layer solutions. While CO_2 recovery efficiencies increase with excess middle-layer solutions supply, the CO_3^{2-} utilization efficiencies remain low for the 0.5 M and 1.0 M K_2CO_3, particularly at current densities higher than 50 mA cm^{-2}.

nature portfolio

Corresponding author(s): Prof. Haotian Wang

Last updated by author(s): Nov 24, 2025

Reporting Summary

Nature Portfolio wishes to improve the reproducibility of the work that we publish. This form provides structure for consistency and transparency in reporting. For further information on Nature Portfolio policies, see our Editorial Policies and the Editorial Policy Checklist.

Statistics

For all statistical analyses, confirm that the following items are present in the figure legend, table legend, main text, or Methods section.

n/a	Confirmed
☐	☒ The exact sample size (*n*) for each experimental group/condition, given as a discrete number and unit of measurement
☐	☒ A statement on whether measurements were taken from distinct samples or whether the same sample was measured repeatedly
☒	☐ The statistical test(s) used AND whether they are one- or two-sided *Only common tests should be described solely by name; describe more complex techniques in the Methods section.*
☒	☐ A description of all covariates tested
☒	☐ A description of any assumptions or corrections, such as tests of normality and adjustment for multiple comparisons
☐	☒ A full description of the statistical parameters including central tendency (e.g. means) or other basic estimates (e.g. regression coefficient) AND variation (e.g. standard deviation) or associated estimates of uncertainty (e.g. confidence intervals)
☒	☐ For null hypothesis testing, the test statistic (e.g. *F*, *t*, *r*) with confidence intervals, effect sizes, degrees of freedom and *P* value noted *Give P values as exact values whenever suitable.*
☒	☐ For Bayesian analysis, information on the choice of priors and Markov chain Monte Carlo settings
☒	☐ For hierarchical and complex designs, identification of the appropriate level for tests and full reporting of outcomes
☒	☐ Estimates of effect sizes (e.g. Cohen's *d*, Pearson's *r*), indicating how they were calculated

Our web collection on statistics for biologists contains articles on many of the points above.

Software and code

Policy information about availability of computer code

Data collection	No custom codes were used in this study. The data was collected with the use of commercially available instruments specified in the Methods section. Namely, EC-lab software v11.46 from BioLogic was used to record electrochemical data, PeakSimple (vPeak495Win10) from SRI instruments or LabSolutions v5.85 was used to record GC data, Bruker TopSpin v3.65 was used to collect the NMR data, Gaslab v2.1 software was used to collect the CO2 censor data.
Data analysis	Once collected, NMR data was processed using MestreNova 12.0.3 software. GC peaks were integrated using integration tool in-built into the PeakSimple (SRI instruments) software. The data was exported and processed in Excel and OriginLab software; the mean and standard deviations were obtained using OriginPro 2018 and OriginPro 2025 in-built statistical analysis tools.

For manuscripts utilizing custom algorithms or software that are central to the research but not yet described in published literature, software must be made available to editors and reviewers. We strongly encourage code deposition in a community repository (e.g. GitHub). See the Nature Portfolio guidelines for submitting code & software for further information.

Data

Policy information about availability of data

All manuscripts must include a data availability statement. This statement should provide the following information, where applicable:

- Accession codes, unique identifiers, or web links for publicly available datasets
- A description of any restrictions on data availability
- For clinical datasets or third party data, please ensure that the statement adheres to our policy

Source Data files contain the data presented in this paper. Extra data supporting the findings is available in the Supplementary Information

Research involving human participants, their data, or biological material

Policy information about studies with human participants or human data. See also policy information about sex, gender (identity/presentation), and sexual orientation and race, ethnicity and racism.

Reporting on sex and gender	*Use the terms sex (biological attribute) and gender (shaped by social and cultural circumstances) carefully in order to avoid confusing both terms. Indicate if findings apply to only one sex or gender; describe whether sex and gender were considered in study design; whether sex and/or gender was determined based on self-reporting or assigned and methods used.* *Provide in the source data disaggregated sex and gender data, where this information has been collected, and if consent has been obtained for sharing of individual-level data; provide overall numbers in this Reporting Summary. Please state if this information has not been collected.* *Report sex- and gender-based analyses where performed, justify reasons for lack of sex- and gender-based analysis.*
Reporting on race, ethnicity, or other socially relevant groupings	*Please specify the socially constructed or socially relevant categorization variable(s) used in your manuscript and explain why they were used. Please note that such variables should not be used as proxies for other socially constructed/relevant variables (for example, race or ethnicity should not be used as a proxy for socioeconomic status).* *Provide clear definitions of the relevant terms used, how they were provided (by the participants/respondents, the researchers, or third parties), and the method(s) used to classify people into the different categories (e.g. self-report, census or administrative data, social media data, etc.)* *Please provide details about how you controlled for confounding variables in your analyses.*
Population characteristics	*Describe the covariate-relevant population characteristics of the human research participants (e.g. age, genotypic information, past and current diagnosis and treatment categories). If you filled out the behavioural & social sciences study design questions and have nothing to add here, write "See above."*
Recruitment	*Describe how participants were recruited. Outline any potential self-selection bias or other biases that may be present and how these are likely to impact results.*
Ethics oversight	*Identify the organization(s) that approved the study protocol.*

Note that full information on the approval of the study protocol must also be provided in the manuscript.

Field-specific reporting

Please select the one below that is the best fit for your research. If you are not sure, read the appropriate sections before making your selection.

☐ Life sciences ☐ Behavioural & social sciences ☒ Ecological, evolutionary & environmental sciences

For a reference copy of the document with all sections, see nature.com/documents/nr-reporting-summary-flat.pdf

Ecological, evolutionary & environmental sciences study design

All studies must disclose on these points even when the disclosure is negative.

Study description	The study primary focus is the analysis of CO2 released in the middle layer of three- and four-chamber PSE electrolyzers and CO2RR at the cathode to perform indirect (bi)carbonate reduction. CO2 concentration, middle layer collection flask outlet gas flow rate, current, voltage, cathode gas outlet flow rate, middle layer solution flow rate, GC and NMR data were recorded at each point, and at least three independent measurements were recorded for the datasets which have error bars reported.
Research sample	Commercial nanoparticles (Bi2O3), synthesized nanoparticles (Cu) carbon paper and chemicals were used in the study as reported in the Methods section.
Sampling strategy	At least 3 independent tests were used for the tests where error bars are reported, according to the accepted practice in the field.
Data collection	Most of the data was collected by V.O. using the software and procedures described in Software and code section, while some data collection was performed by A.E. Copper nanocubes synthesis and TEM was performed by A.L.

Timing and spatial scale	The data was collected between June and December 2024, with additional tests in May-July 2025. For most tests (excluding stability), the test was obtained within a day for a certain datapoint. Stability tests have time as x axis scale.
Data exclusions	No data was excluded from the analysis.
Reproducibility	Reproducibility of the tests was verified by A.E.
Randomization	Commercial nanoparticles (BI2O3) and well-studied synthesized nanoparticles (Cu) were used in this study. Deviation from hand spraying the electrodes using the airgun was minimized by using multiple sprayed electrodes over the study.
Blinding	Blinding does not apply to the current study due to its nature as exploring commercial and well-studied nanoparticles in a specific electrolyzer. However, no distinguishment was made between different hand-sprayed electrodes while testing and data processing to account for the potential variability. The data was processed in a similar fashion across the samples.

Did the study involve field work? ☐ Yes ☒ No

Reporting for specific materials, systems and methods

We require information from authors about some types of materials, experimental systems and methods used in many studies. Here, indicate whether each material, system or method listed is relevant to your study. If you are not sure if a list item applies to your research, read the appropriate section before selecting a response.

Materials & experimental systems

n/a	Involved in the study
☒	☐ Antibodies
☒	☐ Eukaryotic cell lines
☒	☐ Palaeontology and archaeology
☒	☐ Animals and other organisms
☒	☐ Clinical data
☒	☐ Dual use research of concern
☒	☐ Plants

Methods

n/a	Involved in the study
☒	☐ ChIP-seq
☒	☐ Flow cytometry
☒	☐ MRI-based neuroimaging

Plants

Seed stocks	*Report on the source of all seed stocks or other plant material used. If applicable, state the seed stock centre and catalogue number. If plant specimens were collected from the field, describe the collection location, date and sampling procedures.*
Novel plant genotypes	*Describe the methods by which all novel plant genotypes were produced. This includes those generated by transgenic approaches, gene editing, chemical/radiation-based mutagenesis and hybridization. For transgenic lines, describe the transformation method, the number of independent lines analyzed and the generation upon which experiments were performed. For gene-edited lines, describe the editor used, the endogenous sequence targeted for editing, the targeting guide RNA sequence (if applicable) and how the editor was applied.*
Authentication	*Describe any authentication procedures for each seed stock used or novel genotype generated. Describe any experiments used to assess the effect of a mutation and, where applicable, how potential secondary effects (e.g. second site T-DNA insertions, mosiacism, off-target gene editing) were examined.*